Delineating epileptogenic networks using brain imaging data and personalized modeling in drug-resistant epilepsy

Huifang Wang, Marmaduke Woodman, Paul Triebkorn, Jean-Didier Lemarechal, Jayant Jha, Borana Dollomaja, Anirudh Nihalani Vattikonda, Viktor Sip, Samuel Medina Villalon, Meysam Hashemi, et al.

EPILEPSY

Delineating epileptogenic networks using brain imaging data and personalized modeling in drug-resistant epilepsy

Huifang E. Wang[1]*, Marmaduke Woodman[1], Paul Triebkorn[1], Jean-Didier Lemarechal[1,2], Jayant Jha[1], Borana Dollomaja[1], Anirudh Nihalani Vattikonda[1], Viktor Sip[1], Samuel Medina Villalon[1,3], Meysam Hashemi[1], Maxime Guye[4,5], Julia Makhalova[3,4,5], Fabrice Bartolomei[1,3], Viktor Jirsa[1]*

Precise estimates of epileptogenic zone networks (EZNs) are crucial for planning intervention strategies to treat drug-resistant focal epilepsy. Here, we present the virtual epileptic patient (VEP), a workflow that uses personalized brain models and machine learning methods to estimate EZNs and to aid surgical strategies. The structural scaffold of the patient-specific whole-brain network model is constructed from anatomical T1 and diffusion-weighted magnetic resonance imaging. Each network node is equipped with a mathematical dynamical model to simulate seizure activity. Bayesian inference methods sample and optimize key parameters of the personalized model using functional stereoelectroencephalography recordings of patients' seizures. These key parameters together with their personalized model determine a given patient's EZN. Personalized models were further used to predict the outcome of surgical intervention using virtual surgeries. We evaluated the VEP workflow retrospectively using 53 patients with drug-resistant focal epilepsy. VEPs reproduced the clinically defined EZNs with a precision of 0.6, where the physical distance between epileptogenic regions identified by VEP and the clinically defined EZNs was small. Compared with the resected brain regions of 25 patients who underwent surgery, VEP showed lower false discovery rates in seizure-free patients (mean, 0.028) than in non–seizure-free patients (mean, 0.407). VEP is now being evaluated in an ongoing clinical trial (EPINOV) with an expected 356 prospective patients with epilepsy.

INTRODUCTION

Epilepsy is among the most common neurological disorders. The identification of the brain regions [epileptogenic zone (EZ)] involved in the genesis of seizures is necessary before any epilepsy surgery. This identification is based on noninvasive data: magnetic resonance imaging (MRI), positron emission tomography (PET), electroencephalography (EEG), magnetoencephalography (MEG) and, frequently, based on intracerebral recordings, stereoelectroencephalography (SEEG) in particular. Numerous works have shown that epileptogenic regions are more often organized in a network rather than originating from a single epileptic focus (*1*, *2*). SEEG data indicate that epileptogenic networks follow a hierarchical organization, with maximal epileptogenicity in the EZ network (EZN) (*1*). Many methods have been proposed to quantify these EZNs. The epileptogenicity index (EI) quantifies the EZN on the basis of both the spectral and temporal properties of SEEG signals (*3*). The subsequent connectivity EI (cEI) (*4*) combines functional connectivity measure with EI for improving sensitivity of estimation, especially of seizures with slow onset patterns. Statistical parametric mapping was proposed to map EI from SEEG signals anatomically onto the patient's MRI (*5*). Three biomarkers then introduced for EZ identification included fast activity in the frequency band of 80 to 120 Hz together with a very slow transient polarizing shift and voltage depression (*6*). A support vector machine was used to identify a specific time-frequency pattern in the EZ that included a combination of sharp transients or spikes preceded by multiband fast activity concurrent with suppression of lower frequencies (*7*).

Clinical practice requires sophisticated diagnostic approaches and the expertise of trained clinicians to integrate and analyze information from multiple modalities and then determine the EZN. Therefore, methods of causal inference are needed to provide better EZN estimates by naturally integrating multiple modalities to identify the underlying latent mechanisms, which can provide better estimates than those obtained by observation alone. Virtual brains are data-driven dynamical brain network models, which are composed using noninvasively estimated anatomical connectivity from individual participants. The Virtual Brain (TVB) (*8*) is a neuroinformatics platform for the construction and simulation of virtual brains that can provide the required functionality for EZN estimation and make it possible to perform causal inference on the full brain scale.

Here, we introduce the virtual epileptic patient (VEP) workflow, which uses personalized virtual brain models simulated with TVB and machine learning methods by integrating patient-specific anatomical with functional data to aid in clinical decision-making by estimating the EZN and further optimizing surgical strategy. The full brain models are built in a patient-specific space defined by

[1]Aix-Marseille Université, Institut National de la Santé et de la Recherche Médicale, Institut de Neurosciences des Systèmes (INS) UMR1106, Marseille 13005, France. [2]Sorbonne Université, Institut du Cerveau - Paris Brain Institute - ICM, Inserm, CNRS, Centre MEG-EEG and Experimental Neurosurgery team, Paris F-75013, France. [3]APHM, Epileptology and Clinical Neurophysiology Department, Timone Hospital, Marseille 13005, France. [4]Aix-Marseille Université, CNRS, CRMBM, Marseille 13005, France. [5]APHM, Timone University Hospital, CEMEREM, Marseille 13005, France.
*Corresponding author. Email: huyfang.wang@univ-amu.fr (H.E.W.); viktor.jirsa@univ-amu.fr (V.J.)

T1-weighted MRI data (T1-MRI). Neural models are built for each node, which is each vertex of 260,000 in high-resolution neural field models (NFMs) and one brain region of 162 in low-resolution neural mass models (NMMs). Diffusion-weighted MRI (DW-MRI) is used to define a patient's specific connectivity between the nodes. We previously demonstrated that patient-specific nodal connectivity information can improve the estimation of parameters (*9*, *10*). Inferring virtual brain model parameters such that the simulated data match the patient's seizure organization further increases patient specificity. This inference process identifies the EZN using techniques from machine learning, particularly through Markov chain Monte Carlo sampling. This method generates many random samples of model parameters and virtual brain simulations and evaluates these for consistency with empirical data (the patient's functional data from SEEG recording). Inferences can be further improved by integrating prior knowledge about the possible spatial distribution of the EZN, such as that obtained from the spatial extent of MRI-visible anatomical lesions or metabolic abnormalities revealed by PET imaging, as well as from seizure semiology, to reduce uncertainty and to finesse the ill-posed problem of parameter estimation. After the first proof of concept of the VEP (*11*), we studied and tested different modeling methods (*12*–*15*), model inversion methods (*16*–*21*), and surgery strategies (*22*, *23*).

Here, we present a complete and extensively tested VEP workflow to identify EZNs that could potentially be used in clinical practice. We demonstrate in a representative use case how to estimate the patient's EZNs using virtual brain modeling derived from individual T1-MRI, DW-MRI, and SEEG recordings. Furthermore, we performed virtual surgery to predict the outcome of the patient's real surgery. The VEP was tested using a cohort of 53 retrospective patients in the current study. We also developed the concept of degeneracy for uncertainty quantification and subsequent proper use in the clinical context using four types of patients. The VEP workflow provides a foundation for further improvements in both brain modeling and epilepsy studies and is now being evaluated prospectively in a clinical trial (EPINOV NCT03643016) recruiting 356 patients with epilepsy.

RESULTS

VEP workflow

VEP assists in the identification of the EZN based on a personalized whole-brain network model. The model defines the brain as a network of regions, each representing a node in the brain network (see Fig. 1 for workflow and fig. S1 for flowchart). These regions are delineated by the VEP atlas, a cortical and subcortical parcellation of the brain developed for use in epileptology and functional neurosurgery (*24*). The VEP atlas considers region sizes adapted to EZN diagnostics for improved performance of model inversion techniques. Using geometric information and neuroanatomical conventions, brain regions can be automatically labeled based on the patient's T1-MRI. Connections between regions are estimated through streamline tractography from DW-MRI. Together with the brain parcellation from the T1-MRI, this method can provide a patient-specific structural connectivity matrix, which defines the links between the nodes of the network. The dynamics of each node are defined by an NMM, a system of nonlinear differential equations that represents the neural dynamics in that brain region. In this work, we used the Epileptor (*25*), a phenomenological NMM capable of simulating seizure-like activity.

The signals generated by Epileptor models on the brain region level are called source signals. The measured signals from the SEEG electrodes are called sensor signals. To map the simulated sources from the brain regions to the SEEG sensors, the electromagnetic forward problem needs to be solved. Localizing the implanted SEEG electrodes in patient-specific space uses the coregistration of post-SEEG implant computed tomography (CT) with the T1-MRI image. The source-to-sensor map, the so-called gain matrix, is a function of the distance between the sources and sensors (*26*). Brain regions, the connectivity matrix, and the gain matrix are all defined in the patient-specific brain space, which is determined by the T1-MRI images. Note that, in the VEP pipeline, the source space covers the whole brain, specifically 162 brain regions defined by the VEP atlas in the NMM, whereas the sensors only sample part of the brain, depending on the patient-specific SEEG implantation scheme.

The model inversion module allows us to infer the free model parameters by fitting the SEEG data features. The key free model parameters were the excitability ($\boldsymbol{x_0}$) of each brain region and the global connectivity coupling (K), both of which play important roles in defining EZNs. The VEP workflow includes two independent model inversion methods based on Bayesian inference, namely, the optimization and sampling pipelines, which complement each other. The optimization pipeline uses the limited-memory Broyden-Fletcher-Goldfarb-Shanno algorithm (*27*), given prior information and the likelihood function of the data given parameters, to obtain a (local) maximum of the posterior distribution estimate of the model parameters, a so-called maximum a posteriori (MAP). The low computational costs and high robustness of this MAP method allow us to measure the sensitivity of the estimated results in terms of the sampled SEEG sensor space. To do this, 100 MAP estimates are obtained on datasets with a random sensor removed, resulting in a distribution of epileptogenicity values (EVs) for each region. The EV is calculated by considering the seizure delay in the source level activity based on the posterior of the key free parameters including $\boldsymbol{x_0}$ and K. In the sampling pipeline, full Bayesian inference uses a self-tuning variant of the Hamiltonian Monte Carlo (HMC) algorithm to estimate the potential multimodal posterior distributions of the parameters of the personalized NMMs (*28*, *29*). Multiple chains start from different random initial conditions to sample the model parameters from their respective posterior distributions. Because many brain regions are distant from the SEEG recording electrodes in epilepsy, causing the model inversion to become an ill-posed problem, we introduced a reparameterization technique to reorganize the model configuration space to facilitate an efficient exploration of the posterior distribution space in terms of computational time and convergence diagnostics. Unlike the prior covariance constraints based on an eigen-decomposition as in (*30*), we reparameterized the configuration space on the basis of the dominant linear combinations derived from the source-to-sensor map so that the HMC algorithm could put more weight toward efficiently exploring the dominant brain regions in the first few linear combinations.

The inputs of the model inversion module are the data feature and a prior. The envelope of the signal power (high-pass–filtered signal followed by envelope smoothing) from empirical SEEG recordings serves as the data feature. We illustrate the data features

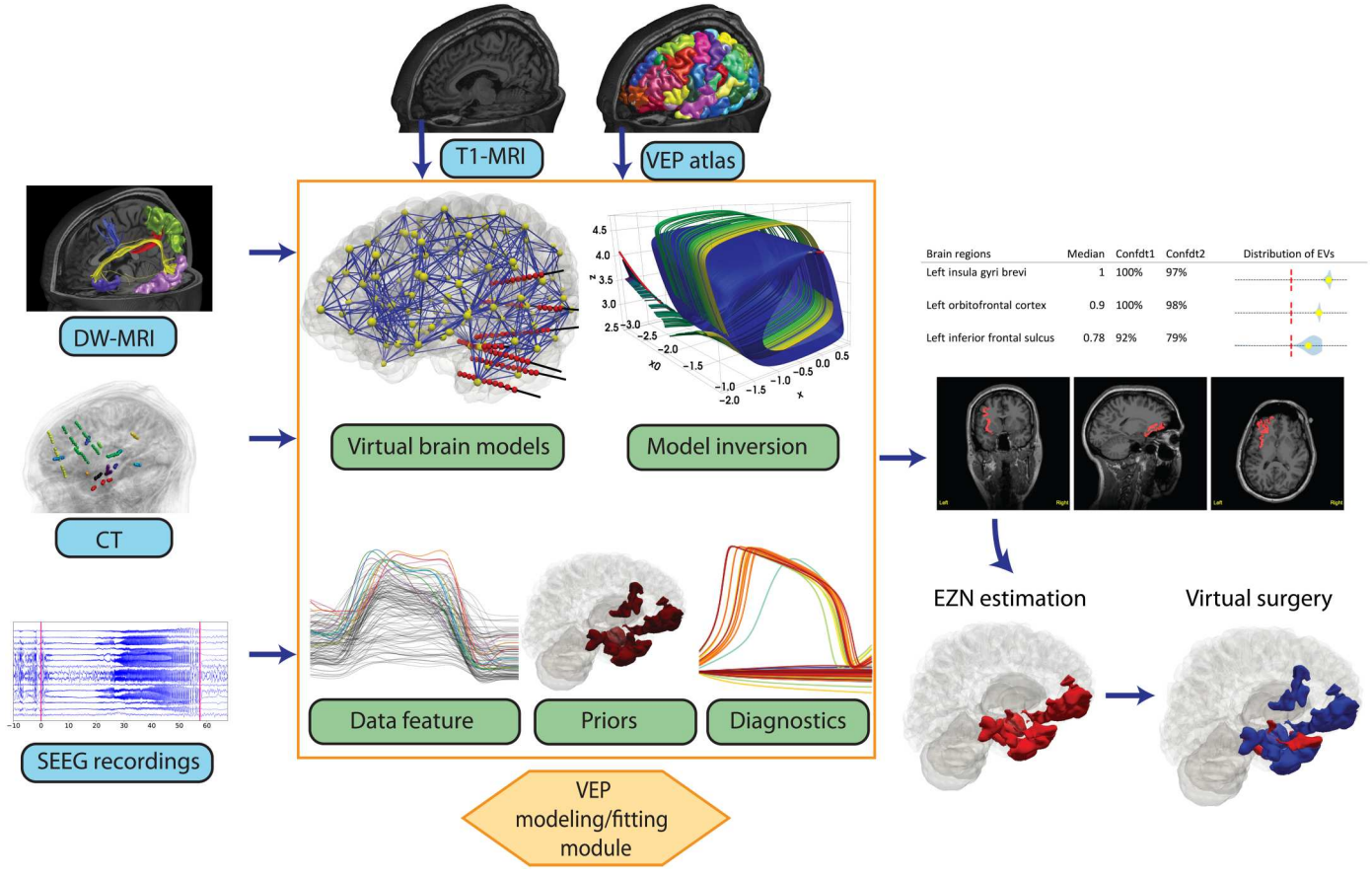

Fig. 1. Workflow of the VEP. A T1-weighted MRI (T1-MRI) is used to extract the individual brain anatomy and to define distinct brain regions according to the VEP atlas. Tractography is performed on diffusion-weighted MRI (DW-MRI) data to estimate the length and density of white matter tracts. These are grouped according to regions obtained from the atlas to derive a structural connectivity matrix that specifies the connection strength between brain regions. A post-SEEG implantation CT scan is used to find the exact locations of the SEEG electrodes and construct the source-to-sensor map using the so-called gain matrix. NMMs at each source location are connected through the connectivity matrix, and the neural source activity is simulated. The gain matrix maps the simulated source activity to the corresponding SEEG signals. Bayesian inference methods are used to estimate the patient-specific parameters of the model based on the data features extracted from SEEG signals and priors from added knowledge, such as analysis of the SEEG data or clinical hypotheses. The output is the suggested EZN, which can be communicated by a distribution table and heatmap in the T1-MRI data. Different virtual surgical strategies can be tested in the personalized model to achieve the best outcome.

from the two patients with the most common seizure onset patterns in fig. S2 (A and B) as well as three patients with other patterns in fig. S3. The prior can be estimated or defined by added knowledge, such as MRI-visible lesions or the clinical EZN hypothesis based on a combination of clinical evidence or extended data analysis from the SEEG signal. We also designed prior estimate algorithms on the basis of delay information from filtered SEEG signals in multiple frequency bands during seizure onset. Please note that the aim of introducing the different priors was to accumulate additional clinical knowledge rather than to perform a methodological model comparison as is done in dynamic causal modeling (DCM) (*31*).

The output of the model inversion module results in a distribution of EVs, which is determined by the key parameters from the model inversion and the patient's structural connectivity. Certain excitability (x_0) values, called bifurcation points, can determine whether the corresponding regions have the potential to generate seizures. The network configurations, including both the structural connectivity itself and the global coupling scale (K), can vary these bifurcation points. Thus, the definition of the EZN in the context of VEP is the network of brain regions with a high degree of excitability under a given connectivity configuration that can lead to a seizure. (For more details, see the "Definition of EZN from a modeling perspective" section in Supplementary Materials and Methods.) An overview of the most relevant brain regions, according to the model estimate based on the EVs, is presented in the VEP clinical report. The report table contains the information from highlighted brain regions with the distribution of the estimated EVs, their median, and the confidence values. In addition, the regions identified by the model as belonging to the EZN are represented in red in the three classical planes in the patient's three-dimensional (3D) T1-MRI images (called a heatmap), provided in a user-friendly viewer. Furthermore, the VEP workflow provides the therapeutic solution by a virtual surgical strategy based on the estimated EZN. Different surgical strategies can be tested to find a minimal resection area to achieve seizure freedom for the patient while minimizing the risk of functional deficits.

In sum, we assumed that brain activity could be captured by whole-brain network models, where the dynamics of brain

regions interact with each other. Both the parameter setting (such as excitability) on each node and connectivity between nodes play important roles in generating seizure activity. Bayesian model inversion provides a natural way to combine prior knowledge and functional data (SEEG data) to obtain the posterior of the parameters and then further to estimate the EZN and virtual surgery. Last, we built a patient-specific brain model from this patient's anatomical and functional data.

Validation on high-resolution synthetic data

Synthetic data can provide the ground truth of the EZN, which we cannot obtain from empirical data. The ground truth of the EZN defines the brain regions demonstrating seizure activities on the source level of the simulated datasets. Thus, synthetic data can be a useful tool for validating VEP pipelines by allowing investigators to compare the ground-truth EZN shown in the simulations with those inferred from the model inversion module. The simulation module of the VEP workflow for generating the synthetic testing data includes both NMMs in low spatial resolution and NFMs in high spatial resolution, where each node element of the model represents an average of ~16 cm^2 and ~1 mm^2 of the cortical surface, respectively. NMMs have proven their efficiency in capturing the main features of brain functional behaviors by accounting for interactions between brain regions (*11*). In epilepsy, they can capture the main features of seizure generation and propagation while considering the underlying connectivity of the network characteristics of seizures. Their low computational cost makes model inversion and parameter inference possible. NMMs can be used for both the simulation and model inversion modules.

NFMs implement field equations representing neural activity in continuous space (*32*), increasing the resolution by a factor of 1000 compared with the discrete point representation of brain regions in NMMs. Neural fields allow the use of detailed connectivity, considering both local, between neighboring points on the field, and global connections, along white matter fibers. Another important advantage of neural field modeling is to provide more realistic source-to-sensor mapping by considering both the orientation and distance between the dipoles and the sensor. Supportive evidence comes from the experimental literature, which has shown that the current dipole is mainly attributable to pyramidal cells in the cortical gray matter and is aligned perpendicular to the surface (*33*).

We validated the VEP using synthetic data generated by the NFMs. We used the 6D Epileptor on each of the 260,000 vertices representing the cortical mesh. The EZN was set to cover three brain regions in the left hemisphere. Figure 2A illustrates the time series in the selected source signals and the signal power, which is mapped on the basis of the brain high-resolution meshes. We observed complex spatial patterns within a brain region in which the seizure onset and offset times were not necessarily synchronized. We generated synthetic SEEG sensor data using the gain matrix while considering both the orientation and distance of the dipoles with respect to the sensors (Fig. 2B). The envelope function of the synthetic SEEG data provided the data feature for the VEP model inversion. Here, the VEP inversion module was based on the NMM, with a lower dimensional model (2D Epileptor), which captures the envelope function, and a low-resolution gain matrix, which considers only the distance between the nodes and sensors (Fig. 2C). On the basis of the distribution of EVs, the EZN was declared. Both the optimization (Fig. 2D) and sampling pipelines (Fig. 2E) identified the ground-truth EZN. To avoid bias from prior knowledge the sampling pipeline used a noninformative prior, that is, we used the same prior distribution with low mean excitability for all brain regions. The clinical table based on the distribution of EVs shows the optimized results from datasets with different SEEG spatial samplings (Fig. 2D). The sampling pipeline used a noninformative prior in which all the brain regions followed the same prior distribution. The posterior distribution of EVs from the sampling pipeline was based on 16 chains starting from eight different optimized initial conditions. Each HMC chain created 500 samples (Fig. 2E). The heatmap projected on the patient's T1-MRI shows the spatial mapping of the EZN (sagittal, axial, and coronal view images shown in Fig. 2F).

EZN estimation using empirical patient data

Next, we applied the VEP workflow to empirical data from a right-handed 29-year-old female patient initially diagnosed with left frontal epilepsy. We first extracted the structural connectivity matrix (fig. S4) and the source-to-sensor map (fig. S5) from individual T1-MRI, DW-MRI, and post-SEEG implantation CT imaging data. Using these along with the data features (fig. S6A) of SEEG seizure recordings as input, we ran both optimization and sampling pipelines. Figure 3A shows the SEEG recording of one seizure, and Fig. 3B demonstrates the distribution of the signal power among all the electrodes in a cortical mesh, with high activity in the frontal and insular cortex. A VEP prior algorithm calculated the sensor prior vector on the basis of 52 different frequency bands from 10 to 110 Hz by taking into account the delay of the seizure onset in each channel (fig. S6B). Two different methods were used to project the prior value from the sensor to the source level: where VEP-M directly maps the prior value of the sensor with the shortest distance to a given source (fig. S7) and where VEP-W maps a weighted sum of the prior values of all sensors to each source based on their distance (fig. S8). We ran the optimization pipeline with four different prior networks: VEP-M (Fig. 3C), VEP-W (fig. S9A), the clinical EZN hypothesis (fig. S9B), and an uninformative prior where all regions have the same probability distribution as the healthy regions (fig. S9**C**). The clinical EZN hypothesis was established by neurologists (J.M. and F.B.) based on visual and quantitative ictal SEEG signal analysis using the EI and integrating interictal data and cortical stimulation results. Comparing the EZN identified from four runs, the left central operculum, which was identified by a noninformative prior, was not identified with the informative priors. To investigate the influence of structural connectivity, we ran the optimization pipeline without considering any connection between brain regions by taking into account an uninformative prior. In this example, we showed that both the left insula gyri brevi and the left orbitofrontal cortex were identified as part of the EZN only when this patient's structural connectivity was considered (fig. S9D).

In the sampling pipeline, we ran the HMC algorithms in 16 chains starting from eight optimized initial conditions. On the basis of the sampled parameters of the NMM, we obtained the simulation that best matched the given data features, as measured by the marginal likelihood. The sampling pipeline used a noninformative prior in which all the brain regions followed the same prior distribution. The posterior distribution of three brain regions (Fig. 3D) confirmed the three brain regions identified by the optimization pipeline. We analyzed four seizures of this patient and integrated

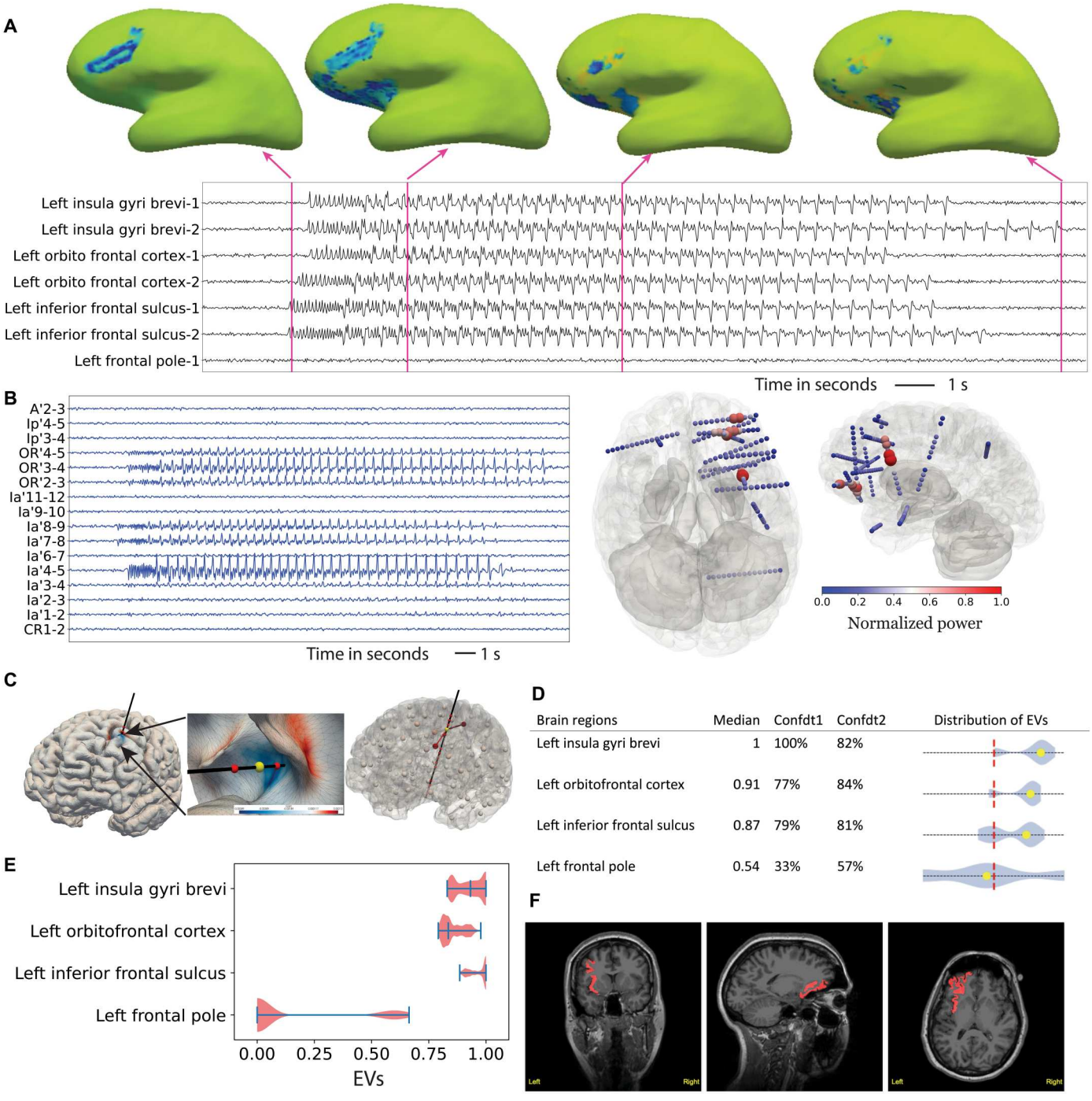

Fig. 2. VEP validation using high-resolution synthetic data. (**A**) Seizure dynamics were simulated using an NFM with an EZN of three given regions in the left hemisphere: left insula gyri brevi, left orbitofrontal cortex, and left inferior frontal sulcus. Neural activity is shown on the inflated cortical mesh at four different time points. The time series of neural activity at seven locations on the mesh are shown below the brain models in (A). (**B**) Synthetic SEEG data were derived by projecting the source activity using the gain matrix. Signal power at each SEEG contact, which is color-coded in a 3D cortical mesh, revealed strong activations in the frontal lobe. (**C**) An NFM, which represents neural activity continuously in space and takes into account the electrical dipole orientation normal to the surface for the forward solution, was used for the simulation of the SEEG data. A computationally feasible reduced NMM was used for model inversion. (**D**) A clinical report table shows the inferred EV distribution and obtained metrics from the optimization pipeline. The given threshold (0.5) is shown by red dashed lines. (**E**) Posterior distribution of EV values from the sampling pipeline. (**F**) The identified EZN is shown in a patient-specific T1-MRI called the heatmap.

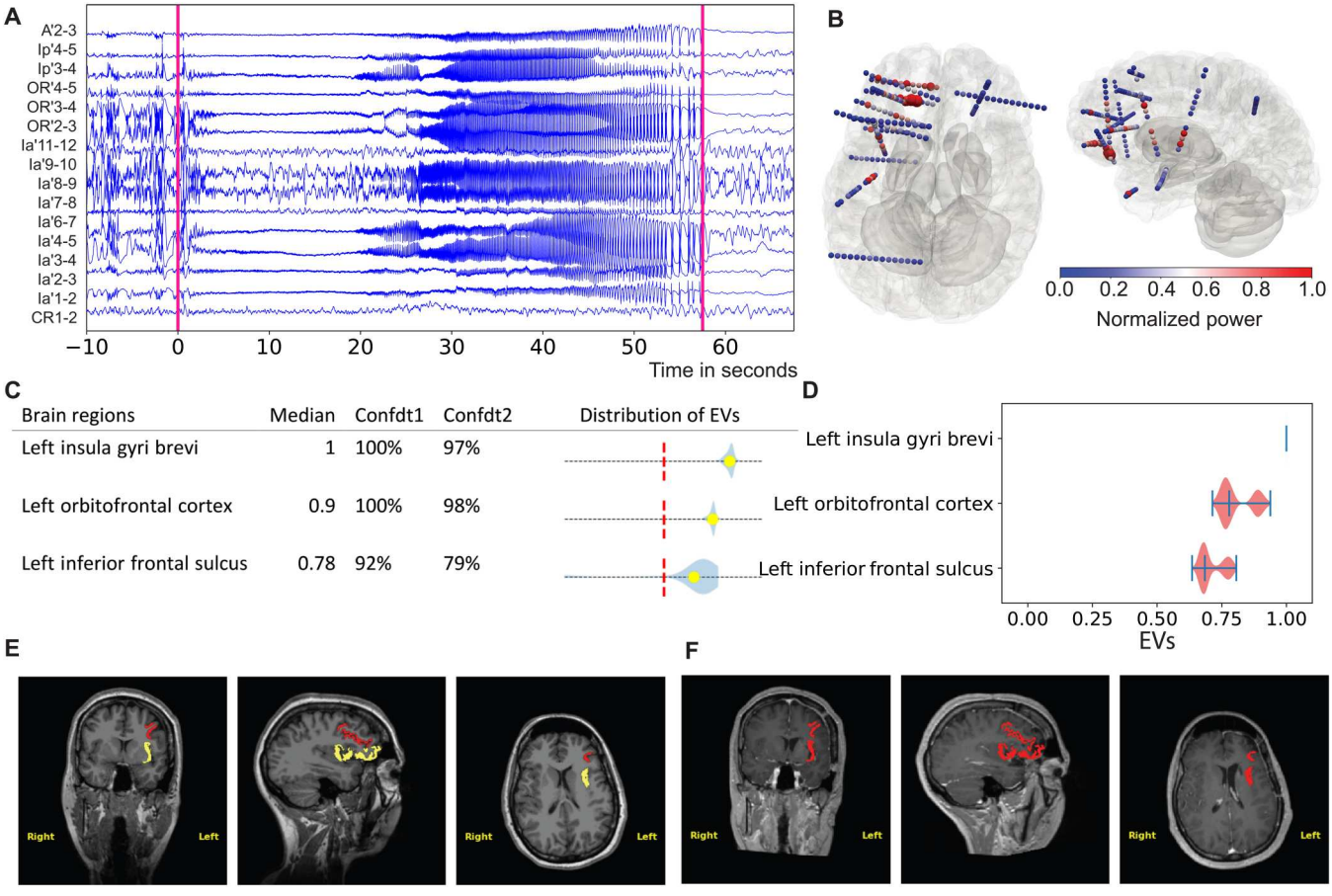

Fig. 3. VEP results for clinical use case. (**A**) Selected SEEG recordings from one seizure of a 29-year-old female patient. (**B**) Distribution of the signal power across contacts inside the cortical mesh from two different perspectives. The sizes and colors of the electrodes indicate signal power. Large size and red color indicate high power. (**C**) Clinical report table from the optimization pipeline. (**D**) Posterior distribution of the EV (higher value indicates higher probability for seizure) for three selected regions obtained from the sampling pipeline. (**E**) Heatmap of the regions identified only by VEP (in red) and the overlapping regions with clinical hypothesis (in yellow), shown in a preoperative T1-MRI. (**F**) Heatmap of the VEP results (in red) shown in a postoperative T1-MRI.

the results of the four seizures to obtain three brain regions as EZNs (fig. S10). The EZN from the clinical hypothesis (the left insula gyri brevi and the left orbitofrontal cortex) and from VEP (the left insula gyri brevi and the left orbitofrontal cortex and the left inferior frontal sulcus) was overlaid onto the presurgical T1-MRI (Fig. 3E) and the postoperative T1-MRI (Fig. 3F). Two of three of the VEP-identified brain regions were also identified by the clinicians. The patient underwent resective surgery aiming the clinically defined EZN, which resulted in a reduction in seizure frequency but did not produce seizure freedom.

VEP virtual surgery module

The estimation of the EZN provides a diagnostic result, whereas a therapeutic solution proposes the surgical intervention, such as the minimum number of brain regions that can be treated to allow seizure control while offering the best functional outcome. We refer to the simulation of different intervention hypotheses as "virtual surgery." Here, we used the same patient as in the section before and worked with the inferred parameters to implement the identified three EZN regions in a VEP simulation (Fig. 4A). The simulated time series and corresponding power distribution are shown in Fig. 4B. For this patient, we tested two virtual surgery hypotheses: removing the two brain regions identified in the clinician hypothesis (Fig. 4, C and D) and removing five brain regions, as was done in the real surgery (Fig. 4, E and F). Comparing the time series before and after the virtual surgery (Fig. 4B versus Fig. 4, D and F), the seizure reduction was obvious, but the patient was not seizure-free, which is consistent with the real surgery outcome. This patient was not seizure-free but with a worthwhile seizure reduction after a surgery that removed the left insula gyri brevi, the left orbitofrontal cortex, the left F3 pars orbitalis, partially the left gyrus rectus, and partially the left F2 rostral. Comparing the time series between the two surgical hypotheses (Fig. 4, D versus F), we saw no notable difference between removing the two brain regions identified by the clinicians and removing five (two plus three additional) brain regions, as in the real surgery. This is not unexpected because none of these three additional regions were identified as EZN, neither by the clinicians nor by VEP. The three additional brain regions in the real surgery were removed to provide access to the brain regions proposed by the neurologists.

Next, we investigated five virtual surgery hypotheses for another patient who had a resective surgery outcome of seizure freedom. We

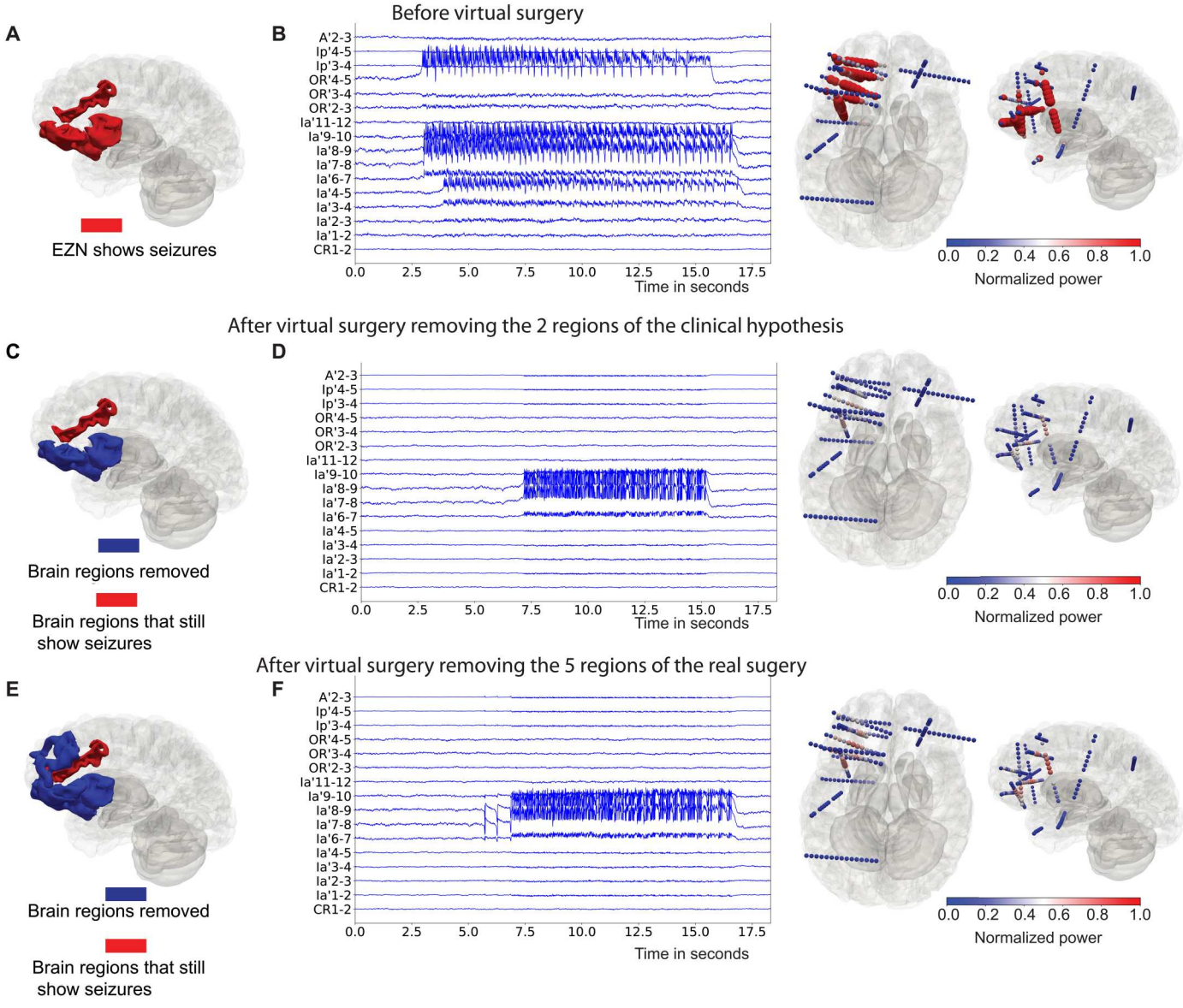

Fig. 4. VEP virtual surgery example. The same patient as in Fig. 3 is shown. (**A** and **B**) Whole-brain simulation before virtual surgery. (A) The EZN (highlighted in red) shows seizures in a 3D brain. The EZN includes the left insula gyri brevi, left orbitofrontal cortex, and left inferior frontal sulcus. (B) Selected simulated SEEG time series using the EZN defined in (A) and the distribution of the signal power across contacts in a 3D brain from two different perspectives of the simulated data. (**C** and **D**) Whole-brain simulation after virtual surgery, removing the two brain regions according to the clinical hypothesis. (C) The left insula gyri brevi and the left orbitofrontal cortex (highlighted in blue) were virtually resected, and the left inferior frontal sulcus (highlighted in red) allowed the seizure activity to remain. (D) Selected simulated SEEG time series after virtual surgery defined in (C) and the corresponding distribution of the signal power across SEEG contacts. (**E** and **F**) Whole-brain simulation after virtual surgery removing the five regions according to the real surgery. (E) The left insula gyri brevi and the left orbitofrontal cortex, the left gyrus rectus, the left F2 rostral, and the left F3 pars orbitalis (highlighted in blue) were resected both virtually and in actuality, and the left inferior frontal sulcus (highlighted in red) allowed the seizure activity to remain. (F) Selected simulated SEEG time series after the virtual surgery defined in (E) and its corresponding distribution of the signal power across SEEG contacts.

first built the simulated model using the VEP results for this patient with the three brain regions identified as the EZN. The simulated data are shown in fig. S11 (A and B). The clinical hypothesis identified seven regions in the right frontal and temporal regions as the EZN. If all of them were to be removed, then the virtual surgery suggested that there would be reduced seizure amplitude but still no seizure freedom (fig. S11, C to E). Nineteen brain regions were removed in real surgery to achieve seizure-free status, and the virtual surgery was consistent with the outcome of the actual surgery (fig. S11, F to H). This is not unexpected given such a large and redundant number of regions in the surgical resection. Then, we considered two scenarios in terms of the global connectivity scale K. In the first scenario when K was large, which could mean that the patient would be in a situation with fewer seizure triggers or with some anti-epilepsy drug, removing four regions was sufficient for seizure freedom (fig. S12A). In the second scenario

in which K was smaller, removing a minimum of six regions led to seizure freedom (fig. S12, B and C), but removing four regions was not sufficient.

VEP evaluation module

The performance of the VEP workflow in estimating the EZN for individual patients was quantified by evaluating the inferred EZN against the clinical hypothesis or surgical resection as assessed by postoperative MRI (Fig. 5A). The commonly used seven metrics for the evaluation are based on true/false-positive/negative EZ classifications for each brain region on the basis of presurgical evaluation. Compared with the clinical hypothesis, the predictive power of VEPs for a cohort of 53 retrospective patients (Fig. 5B) showed good precision (mean, 0.613) and acceptable recall (mean, 0.478) when a fixed threshold (0.5) was set for all patients. We also calculated the $F_{0.5}$ (mean, 0.573), which is the weighted mean of the precision and recall with double weight on precision. If we used a personalized threshold, then we obtained a higher precision (mean, 0.769) and $F_{0.5}$ (mean, 0.652). We also introduced two threshold-free measures: the average precision score (with mean of 0.443) and the area under receiver operating characteristic curve (with mean of 0.761). Although a discrepancy existed between the VEP and the clinical hypothesis, the physical distance of each epileptogenic region identified by the VEP to all the EZs comprising the clinical hypothesis was small (mean, 5.67 mm; Fig. 5C). We also evaluated VEP model performances in terms of MRI-visible lesion and EZN topography using precision and recall with fixed thresholds and using precision and $F_{0.5}$ with personalized thresholds. All measures demonstrated slightly higher values in patients with normal MRI than in those with an MRI-visible structural abnormality (fig. S13). In terms of EZN topography, all measures demonstrated a slight difference in the order of temporal (highest), temporal-plus (*34*, *35*), and extratemporal (lowest) (fig. S14).

When the VEP results were compared with the resected brain regions, we used the false discovery rate (FDR) as a performance metric in which false positives become more important. With seizure-free patients, it is reasonable to assume that the EZN was completely removed and that thus a false-positive estimate has a high possibility of being really outside the EZN, whereas in non–seizure-free patients, a false-positive estimate has a high possibility of corresponding to the nonresected epileptogenic regions that would cause the seizures to remain. The VEP showed a very small FDR (mean, 0.028) for seizure-free patients (Fig. 5D) compared with the EI (where we simply projected the EI results automatically to the VEP regions; mean, 0.149). For the non–seizure-free group, the VEP results showed a large increase in the FDR (mean, 0.407) compared with the seizure-free patients, suggesting that it may be possible to better exploit the predictive power of the VEP. Please note that a very large resection extent in some patients also contributed to the low FDR value to a certain degree.

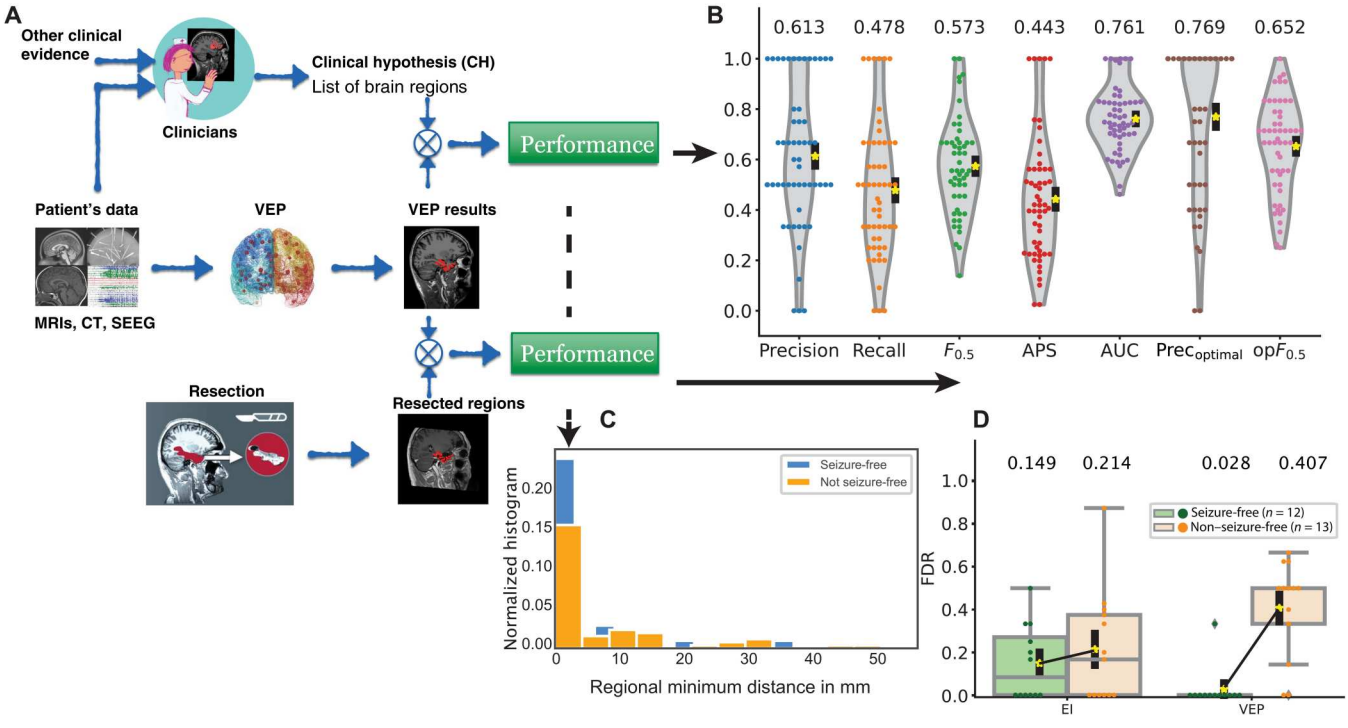

Fig. 5. Performance of VEP. (**A**) The evaluation framework includes two blocks. Top: The VEP results were evaluated against the clinical hypothesis on the basis of a presurgical assessment by clinicians. Bottom: The VEP results were evaluated against resected brain regions in the postoperative MRI. (**B**) Distribution of the seven statistical evaluation results for 53 patients: precision, recall, $F_{0.5}$, average precision score (APS), the area under receiver operating characteristic curve (AUC), $Prec_{optimal}$, and $opF_{0.5}$. For each measure, a violin plot demonstrates the distribution of 53 patients, with each dot representing a patient. Above each violin plot is the mean value of a statistical measure across the 53 patients. The yellow stars and black bars are mean values ±SEM. (**C**) Histogram of the minimal distance between each identified VEP region and the clinical hypothesis in the two groups in terms of surgical outcome, that is, seizure-free versus non–seizure-free. (**D**) False discovery rate (FDR) of the epileptogenicity index (EI) and VEP against postoperative MRI for 12 seizure-free patients and 13 non–seizure-free patients. Above each box plot is the mean value of the FDR. Yellow stars and black bars are mean values ±SEM.

Interpretation of VEP

Degeneracy, the ability of structurally different elements to yield the same function or behavior, is a natural property of the brain system (*36*, *37*). In the context of VEP workflow, degeneracy occurs when the different parameter sets (different EZNs) in the underlying brain modeling lead to the same seizure patterns, which we can observe in SEEG recordings, or one parameter set can lead to the different seizure patterns due to different brain states. We investigated two main reasons for degeneracy: (i) insufficient SEEG recordings and (ii) high dimensionality and nonlinearity of the brain's intrinsic nature. The first investigation helped us to better understand the risk of identifying false EZNs from the SEEG implementation, whereas the second investigation used degeneracy to improve our interpretation of the VEP results for clinical use.

We used the same high-resolution synthetic data from our first example patient, from whom we had three regions in the EZN. We demonstrated the VEP performance from the sampling pipeline with removed electrodes (Fig. 6A). We used the weighted average F1 score to quantify VEP performance based on the posterior distributions of EVs for each dataset with removed electrodes (fig. S15). On the basis of the F1 score, the most important electrode, Ia′, targeted two of three EZN regions (the left insula gyri brevi and the left inferior frontal sulcus). Then, the second most important electrode, FT′, was targeted in one EZN region, followed by some electrodes in the neighborhood of the EZN. Electrodes OR′ and R′, targeted in the same region (the left orbitofrontal cortex), have different effects due to different implantation locations and orientations and also due to their combination with other electrodes. In terms of model prediction, missing both is worse than missing one of them. Then, we demonstrated how to use the VEP sampling pipeline to verify the possible sufficient implanted electrodes for a given EZN. We started to build the possible sufficient implanted electrodes by adding them one by one according to the sorted important electrodes (Fig. 6A). On the basis of the F1 score and shrinkage of VEP performance (Fig. 6B; posterior distributions of EVs in fig. S16), we identified a sufficient implantation set of four depth electrodes. If electrode OR′ in this set was replaced by electrode R′, then there was another possible sufficient implantation set with six electrodes (Fig. 6B; posterior distributions of EVs in fig. S17).

Next, we used the concept of degeneracy for a proper interpretation of VEP within the clinical context. We assumed that the implantation of SEEG electrodes was not the cause of degeneracy here. We illustrated the results from the sampling HMC pipeline of the VEP on the empirical SEEG recordings from four patients in four cases. In case 1, the patient only showed one seizure type from the

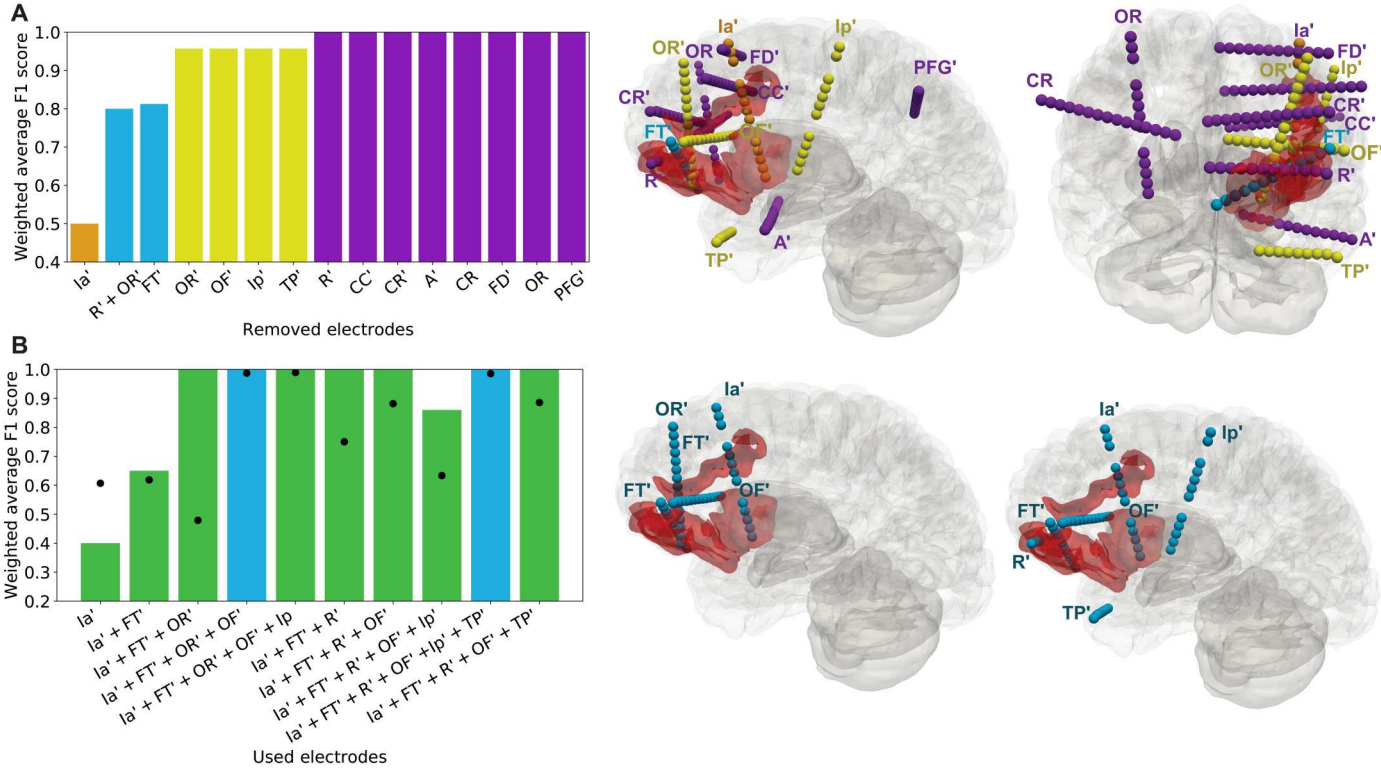

Fig. 6. VEP performance on selected electrodes and the importance of SEEG electrodes. The same patient as in Figs. 2 to 4 is shown. (**A**) VEP performance based on weighted average F1 score on the datasets in which the given electrodes were removed. We classified the electrodes into four groups according to F1 score, with different colors, consistent with electrodes colors in the 3D brains in the right panel. For example, orange corresponds to the lowest F1 score, and its electrode Ia′ has the most important role in identifying the EZN. The EZN includes three regions: the left insula gyri brevi, the left orbitofrontal cortex, and the left inferior frontal sulcus, which are highlighted in red. (**B**) VEP performance based on weighted average F1 score when using only the data features from the selected electrodes. The selected electrodes are listed in the horizontal axis. Black dots show the shrinkage in the VEP performance. The two blue bars correspond to the possible combination with the minimal number of electrodes with high F1 score and shrinkage values while considering OR′ and R′, respectively. The corresponding SEEG implantation schemes are shown in the right panel.

SEEG recordings, and VEP identified only one EZN in Fig. 7A. In this case, the observed SEEG data strongly suggest a single EZN with confidence, although other EZNs may exist according to not-yet-observed recordings. In case 2, the same observed SEEG data suggest several possible EZNs (for example, two possible EZNs in Fig. 7B). In this case, both identified EZNs were capable of explaining the observed SEEG recording due to degeneracy, that is, the different parameter sets of VEP with these different EZNs can generate the similar data features as those from SEEG recording. For clinical decision-making to specify a more reasonable EZN, we need additional data features such as inter-ictal data and the topography of an epileptogenic brain lesion. In our methodology, we can put these pieces of information as informative priors or integrate them as data features. In cases 3 and 4, the patients' SEEG recordings demonstrate different types of seizures. Case 3 illustrates a patient who has two types of seizures, and the VEP identified a different EZN for each type (Fig. 7C). A possible hypothesis here is that a larger EZN exists such that different types of SEEG recording could lead us to discovery of a subset of this EZN. In case 4, the VEP identified the same EZN from two different types of seizure recordings (Fig. 7D). A hypothesis here is that the same EZN produces multiple seizure patterns because of the nonlinearity of the complex brain system, such as the different initial conditions due to the different brain states.

DISCUSSION

VEP is a multimodal probabilistic framework for a personalized end-to-end analysis of brain imaging data from patients with drug-resistant epilepsy. The VEP workflow provides all the necessary and optimized modules using the NMMs to estimate the EZN and provide a virtual surgery strategy in drug-resistant epilepsy. All the modules are state of the art and well tested. Compared with traditional EZN quantification methods based on spectral analysis of SEEG signals, such as the EI (*3*), cEI (*4*), epileptogenicity map (*5*), and EZ fingerprint (*7*), the VEP workflow provides a successful use of brain models. Compared with other model-based methods, such as neural fragility (*38*) and dynamic network biomarker (*39*) based on stability concepts in complex systems theory (*16*), the VEP provides the fully nonlinear system analysis of whole-brain NMMs and works on the whole-brain source spaces instead of on the sensor recording spaces alone. Here, we have provided a full definition of the EZN from a modeling perspective and the corresponding calculations. Both the full sampling of the HMC in Bayesian inference and the neural field high-resolution simulation are state of the art. The current VEP has been extensively tested using a cohort of 53 retrospective patients and is now being evaluated prospectively in a large French clinical trial (EPINOV NCT03643016) recruiting 356 patients from 11 epilepsy centers. The main objective of EPINOV is to evaluate the capacity of the VEP algorithms to improve clinical outcomes in patients suffering from focal drug-resistant epilepsy undergoing SEEG surgery.

Other studies have shown that the EZN is highly correlated with the brain structural lesions observed in MRI (*40*). In addition, certain neurotransmitters and glucose showed hypometabolism in the EZN, as shown by PET studies (*41*). These additional pieces of prior knowledge could be integrated into the VEP workflow by defining the prior distribution. DCM is a general framework that allows for the analysis and variational Bayesian inversion of NMMs (*42*). Using DCM, two related studies investigated the fluctuation of synaptic parameters (*43*) or synaptic coupling weights (*44*) to understand the generation of seizure activities. Compared with VEP, the studies using DCM were based on a small number of cortical regions, and the nonlinear NMM was approximated by its linearization.

Recent studies have demonstrated the advantages of brain modeling in aiding epilepsy surgery by using personalized information and by capably comparing different strategies in silico (*18*, *22*, *23*, *45*–*47*). The virtual surgery module in the VEP workflow provides an all-in-one solution, which uses the generative function of large-scale brain modeling in TVB, a personalized connectome, and a patient-specific estimate of the EZN and its parameters from the VEP diagnostic modules. Here, we only assessed surgical resection, but the VEP generative function has the potential to offer further advice about the type of intervention, such as stimulation, lesionectomy, or laser interstitial thermal therapy, by simulating the optimized brain models under different intervention conditions by varying its corresponding parameters.

Here, we used synthetic data to validate the VEP pipelines because the ground-truth EZN is known by our settings. The parameter sets including the ground-truth EZN are used for generating synthetic data, and, first, we needed to distinguish them from the estimated parameters of the model inversion and also from all other generated parameters in virtual surgery. We are also working on high-dimensional complex systems with many free parameters, which lead to a high level of degeneracy; for example, multiple parameter sets can generate the same data feature as the synthetic data. Thus, from VEP, we may obtain the estimated parameters that may or may not coincide with the generating parameters, but, in both cases, they can generate the data with similar data features as the fitting data features. In this sense, validating on synthetic data can only show the goodness of the VEP performance, but not its weaknesses.

VEP has its limitations. Model-based approaches are usually computationally expensive and parameter-sensitive, which poses challenges for practical use in clinical routine that need to be addressed in the future. Additional limitations include the dynamic nature of the epileptic disorder itself in any given patient over long time scales, which is not considered in VEP. Such changes may display irregular and regular daily to monthly patterns in seizure occurrence, often revealing circadian (*48*, *49*) and cluster organization (*50*). In addition, neural mass modeling approaches reduce thousands of vertices of source activity into one node mapped to a VEP region. Any such grouping cancels out the directionality of the current dipole of the folded cortical sheet, which may lead to incorrect mapping from sources to sensors and thus possibly introduce errors into the estimation of the EZN. The solution is to use model inversion on the high resolution of NFM data. For any inference method, the huge dimensions are a big challenge that needs to be overcome in the future. Meanwhile, we are systematically assessing the ability of the current VEP pipeline of the NMM with the synthetic data from NFM to try to answer two fundamental questions: whether the neural mass version of the VEP pipeline is good enough to identify the ground truth, which was used in the generated data from the NFM, and under which conditions the VEP in the NMM version would succeed or fail.

Introducing regional variance may provide another fundamental way to improve the VEP pipeline. Now, identical parameterization,

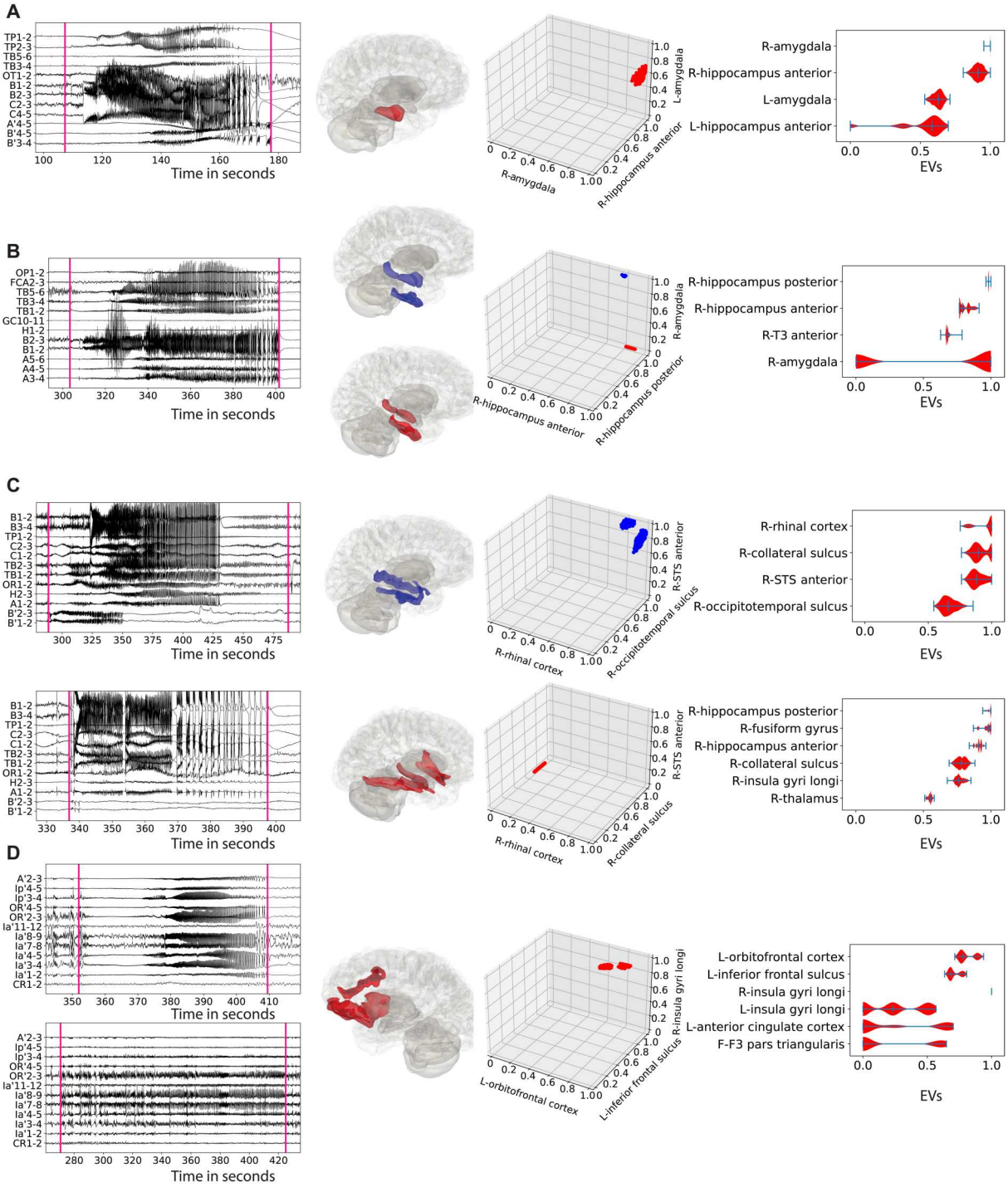

Fig. 7. Four cases for proper interpretation of VEP in clinical use. (**A** to **D**) Each case from left to right: The example of the SEEG recording, the identified EZN(s) highlighted in red/blue for distinguishing the different EZNs in different colors, the EV distribution for selected three regions, and the EV distribution of more selected regions, where R/L is for the right and left hemisphere, respectively. (B and C) Two EZNs are distinguished as red and blue, which correspond to the same color in the 3D EV distribution. (A) Case 1: One EZN identified by the VEP sampling pipeline from one type of SEEG recordings. The identified EZN includes the right amygdala and the right hippocampus anterior. (B) Case 2: Two EZNs identified from the same SEEG recording, with high EVs of the right hippocampus anterior and posterior and the T3 anterior. The EVs of the right amygdala show a bimodal distribution. This suggests two possible different EZNs, one with the right amygdala (in blue) and one without (in red). (C) Case 3: Two distinct EZNs identified from two types of two different SEEG recordings with different spatiotemporal dynamics and the VEP identified a different EZN for each recording type. For the first recorded seizure, the EZN includes the right rhinal cortex, the right collateral sulcus, the right STS anterior, and the right occipitotemporal sulcus (in blue). The second identified EZN includes the right hippocampus anterior and posterior, the right fusiform gyrus, the right collateral sulcus, and the right insula gyri longi (in red). (D) Case 4: One EZN identified from two types of SEEG recordings. The identified EZN includes left insula gyrus brevi, orbitofrontal cortex, and inferior frontal sulcus.

with the exception of the excitability parameter related to seizure generation, is assumed across all sites of the brain. The connectivity network is another element that can influence the regional variance because of different connection strengths. However, the rich repertoire of anatomical data shows differences in cell type, cell architecture, receptor density, and functional specialization between brain areas (*51*, *52*). Some individual-specific 23Na imaging data indicated different degrees of excitability of different brain areas, which could be used to construct more individual-specific models (*53*). This regional variance has been also demonstrated using the power spectra and peak frequencies of functional data, such as SEEG (*24*, *54*). The big challenge is to find a meaningful mapping from the empirical data to the parameters in the neural model. In addition, because most anatomical and functional data about regional variance are available only on the group level, the balance between group and personalized information remains an important issue.

Both scientists and clinicians are now searching for equally efficient noninvasive approaches for diagnosis and treatment in the future for patients with epilepsy who need invasive surgical implantation and intervention today. Toward this purpose, the personalized whole-brain network modeling could play an important role in diagnostic and therapeutic solutions. For diagnostic solutions, the VEP pipeline could integrate the data features of the interictal periods such as an interictal spike or the dynamics of functional connectivity. These data can be recorded by noninvasive recordings such as MEG, EEG, and functional MRI. For therapeutic solutions, brain modeling can predict and access the performance of noninvasive stimulations such as transcranial direct current stimulation or temporal interference. The challenge here is to build realistic models based on an understanding of the stimulation mechanism. All these further adventures in high resolution, regional variance, and noninvasive treatment are based on the VEP workflow that we introduced here.

MATERIALS AND METHODS

Study design

The objective of this study was to develop and evaluate the VEP workflow for estimating EZNs and predicting virtual surgery outcomes for patients with epilepsy. To do so, we collected a dataset comprising 53 retrospective patients with drug-resistant focal epilepsy who underwent a standard presurgical protocol at La Timone Hospital in Marseille, France. Informed written consent was obtained for all patients in compliance with the ethical requirements of the Declaration of Helsinki, and the study protocol was approved by the local ethics committee (Comité de Protection des Personnes sud Méditerranée 1). All patients underwent comprehensive presurgical assessment, which included medical history, neurological examination, neuropsychological assessment, neurological examination, fluorodeoxyglucose PET, high-resolution 3T MRI, long-term scalp EEG, and invasive SEEG recordings. The patients' clinical data are given in table S1. The whole-brain models of VEP were run on patient-specific brain space and connectome, which were defined from noninvasive T1-MRI and DW-MRI images of individual patients. The key parameters related to EZNs were inferred from invasive SEEG recordings. To evaluate the performance of the VEP workflow, we compared the inferred EZN from VEP against the clinical hypothesis of 53 patients or surgical resection as assessed by postoperative MRI of 25 patients who underwent epilepsy surgery. Clinical hypotheses were obtained from presurgical assessment. Surgical outcome was assessed according to Engel classification. The principles of the STARD (standards for reporting diagnostic accuracy studies) guidelines were followed.

Patient data

For each patient with epilepsy, the evaluation included noninvasive T1-MRI (magnetization-prepared rapid acquisition with gradient echo sequence, repetition time of 1.9 or 2.3 s, echo time of 2.19 or 2.98 ms, and voxel size of 1.0 mm by 1.0 mm by 1.0 mm) and DW-MRI images (either with an angular gradient set of 64 directions, repetition time of 10.7 s, echo time of 95 ms, voxel size of 1.95 mm by 1.95 mm by 2.0 mm, and b-weighting of 1000 s/mm^2; or with an angular gradient set of 200 directions, repetition time of 3s, echo time of 88 ms, voxel size of 2.0 mm by 2.0 mm by 2.0 mm, and b-weighting of 1800 s/mm^2). The images were acquired on a Siemens Magnetom Verio 3T MRI scanner. All patients had invasive recordings of SEEG obtained by implanting multiple depth electrodes, each containing 10 to 18 contacts (2 mm long) and separated by 1.5- or 5-mm contact spacing. The SEEG signals were acquired on a 128-channel Deltamed/Natus system with at least a 512-Hz sampling rate and recorded on a hard disk (16 bits per sample) using no digital filter. Two hardware filters were present in the acquisition procedure: a high-pass filter (cutoff frequency equal to 0.16 Hz at −3 dB) and an anti-aliasing low-pass filter (cutoff at one-third of the respective sampling frequency). After the electrode implantation, a cranial CT scan was performed to obtain the location of the implanted electrodes.

Statistical analysis

All data are reported as mean or median values ± SD or SEM, as indicated. The model inversion model of VEP is based on Bayesian inference, which is a statistical inference in which Bayes' theorem is used to update the probability of a hypothesis. Thus, we used the statistical probability to describe key components such as prior, posterior, and model evidence. The performance measures that we used are also based on a hypothesis-testing approach from statistics. Detailed descriptions of all related statistical analysis are provided in their respective sections above. Primary data are provided in data file S1.

Supplementary Materials

This PDF file includes:
Materials and Methods
Figs. S1 to S17
Tables S1 and S2
References (*57*–*67*)

Other Supplementary Material for this manuscript includes the following:
Data file S1
MDAR Reproducibility Checklist

View/request a protocol for this paper from *Bio-protocol*.

REFERENCES AND NOTES

1. F. Bartolomei, S. Lagarde, F. Wendling, A. McGonigal, V. Jirsa, M. Guye, C. Bénar, Defining epileptogenic networks: Contribution of SEEG and signal analysis. *Epilepsia* **58**, 1131–1147 (2017).
2. H. Stefan, F. H. Lopes da Silva, Epileptic neuronal networks: Methods of identification and clinical relevance. *Front. Neurol.* **4**, 8 (2013).
3. F. Bartolomei, P. Chauvel, F. Wendling, Epileptogenicity of brain structures in human temporal lobe epilepsy: A quantified study from intracerebral EEG. *Brain* **131**, 1818–1830 (2008).
4. A. Balatskaya, N. Roehri, S. Lagarde, F. Pizzo, S. Medina, F. Wendling, C.-G. Bénar, F. Bartolomei, The "Connectivity Epileptogenicity Index " (cEI), a method for mapping the different seizure onset patterns in StereoElectroEncephalography recorded seizures. *Clin. Neurophysiol.* **131**, 1947–1955 (2020).
5. O. David, T. Blauwblomme, A.-S. Job, S. Chabardès, D. Hoffmann, L. Minotti, P. Kahane, Imaging the seizure onset zone with stereo-electroencephalography. *Brain* **134**, 2898–2911 (2011).
6. V. Gnatkovsky, M. de Curtis, C. Pastori, F. Cardinale, G. Lo Russo, R. Mai, L. Nobili, I. Sartori, L. Tassi, S. Francione, Biomarkers of epileptogenic zone defined by quantified stereo-EEG analysis. *Epilepsia* **55**, 296–305 (2014).
7. O. Grinenko, J. Li, J. C. Mosher, I. Z. Wang, J. C. Bulacio, J. Gonzalez-Martinez, D. Nair, I. Najm, R. M. Leahy, P. Chauvel, A fingerprint of the epileptogenic zone in human epilepsies. *Brain* **141**, 117–131 (2018).
8. P. Sanz-Leon, S. A. Knock, A. Spiegler, V. K. Jirsa, Mathematical framework for large-scale brain network modeling in The Virtual Brain. *Neuroimage* **111**, 385–430 (2015).
9. F. Melozzi, E. Bergmann, J. A. Harris, I. Kahn, V. Jirsa, C. Bernard, Individual structural features constrain the mouse functional connectome. *Proc. Natl. Acad. Sci. U.S.A.* **116**, 26961–26969 (2019).
10. M. Hashemi, A. N. Vattikonda, V. Sip, S. Diaz-Pier, A. Peyser, H. Wang, M. Guye, F. Bartolomei, M. M. Woodman, V. K. Jirsa, P. N. Taylor, On the influence of prior information evaluated by fully Bayesian criteria in a personalized whole-brain model of epilepsy spread. *PLOS Comput. Biol.* **17**, e1009129 (2021).
11. V. K. Jirsa, T. Proix, D. Perdikis, M. M. Woodman, H. Wang, J. Gonzalez-Martinez, C. Bernard, C. Bénar, M. Guye, P. Chauvel, F. Bartolomei, The virtual epileptic patient: Individualized whole-brain models of epilepsy spread. *Neuroimage* **145**, 377–388 (2017).
12. T. Proix, A. Spiegler, M. Schirner, S. Rothmeier, P. Ritter, V. K. Jirsa, How do parcellation size and short-range connectivity affect dynamics in large-scale brain network models? *Neuroimage* **142**, 135–149 (2016).
13. T. Proix, V. K. Jirsa, F. Bartolomei, M. Guye, W. Truccolo, Predicting the spatiotemporal diversity of seizure propagation and termination in human focal epilepsy. *Nat. Commun.* **9**, 1088 (2018).
14. V. Sip, M. Guye, F. Bartolomei, V. Jirsa, Computational modeling of seizure spread on a cortical surface. *J. Comput. Neurosci.* **50**, 17–31 (2021).
15. V. Sip, J. Scholly, M. Guye, F. Bartolomei, V. Jirsa, P. N. Taylor, Evidence for spreading seizure as a cause of theta-alpha activity electrographic pattern in stereo-EEG seizure recordings. *PLOS Comput. Biol.* **17**, e1008731 (2021).
16. T. Proix, F. Bartolomei, M. Guye, V. K. Jirsa, Individual brain structure and modelling predict seizure propagation. *Brain* **140**, 641–654 (2017).
17. M. Hashemi, A. N. Vattikonda, V. Sip, M. Guye, F. Bartolomei, M. M. Woodman, V. K. Jirsa, The Bayesian Virtual Epileptic Patient: A probabilistic framework designed to infer the spatial map of epileptogenicity in a personalized large-scale brain model of epilepsy spread. *Neuroimage* **217**, 116839 (2020).
18. V. Sip, M. Hashemi, A. N. Vattikonda, M. M. Woodman, H. Wang, J. Scholly, S. M. Villalon, M. Guye, F. Bartolomei, V. K. Jirsa, D. Marinazzo, Data-driven method to infer the seizure propagation patterns in an epileptic brain from intracranial electroencephalography. *PLOS Comput. Biol.* **17**, e1008689 (2021).
19. A. N. Vattikonda, M. Hashemi, V. Sip, M. M. Woodman, F. Bartolomei, V. K. Jirsa, Identifying spatio-temporal seizure propagation patterns in epilepsy using Bayesian inference. *Commun. Biol.* **4**, 1244 (2021).
20. J. Makhalova, S. Medina Villalon, H. Wang, B. Giusiano, M. Woodman, C. Bénar, M. Guye, V. Jirsa, F. Bartolomei, Virtual epileptic patient brain modeling: Relationships with seizure onset and surgical outcome. *Epilepsia* **63**, 1942–1955 (2022).
21. J. Jha, M. Hashemi, A. N. Vattikonda, H. Wang, V. Jirsa, Fully Bayesian estimation of virtual brain parameters with self-tuning Hamiltonian Monte Carlo. *Mach. Learn. Sci. Technol.* **3**, 035016 (2022).
22. S. An, F. Bartolomei, M. Guye, V. Jirsa, D. Marinazzo, Optimization of surgical intervention outside the epileptogenic zone in the Virtual Epileptic Patient (VEP). *PLOS Comput. Biol.* **15**, e1007051 (2019).
23. S. Olmi, S. Petkoski, M. Guye, F. Bartolomei, V. Jirsa, Controlling seizure propagation in large-scale brain networks. *PLOS Comput. Biol.* **15**, e1006805 (2019).
24. H. E. Wang, J. Scholly, P. Triebkorn, V. Sip, S. Medina Villalon, M. M. Woodman, A. Le Troter, M. Guye, F. Bartolomei, V. Jirsa, VEP atlas: An anatomic and functional human brain atlas dedicated to epilepsy patients. *J. Neurosci. Methods* **348**, 108983 (2021).
25. V. K. Jirsa, W. C. Stacey, P. P. Quilichini, A. I. Ivanov, C. Bernard, On the nature of seizure dynamics. *Brain* **137**, 2210–2230 (2014).
26. J. Sarvas, Basic mathematical and electromagnetic concepts of the biomagnetic inverse problem. *Phys. Med. Biol.* **32**, 11–22 (1987).
27. J. Nocedal, S. J. Wright, *Numerical Optimization* (Springer, 2 ed., 1999).
28. B. Carpenter, A. Gelman, M. D. Hoffman, D. Lee, B. Goodrich, M. Betancourt, M. Brubaker, J. Guo, P. Li, A. Riddell, Stan: A probabilistic programming language. *J. Stat. Softw.* **76**, 1–32 (2017).
29. M. Betancourt, A Conceptual Introduction to Hamiltonian Monte Carlo. arXiv:1701.02434 (2017).
30. A. Razi, M. L. Seghier, Y. Zhou, P. McColgan, P. Zeidman, H.-J. Park, O. Sporns, G. Rees, K. J. Friston, Large-scale DCMs for resting-state fMRI. *Netw. Neurosci.* **1**, 222–241 (2017).
31. K. Friston, T. Parr, P. Zeidman, Bayesian model reduction. arXiv:1805.07092 (2018).
32. V. K. Jirsa, Neural field dynamics with local and global connectivity and time delay. *Philos. Trans. R. Soc. A Math. Phys. Eng. Sci.* **367**, 1131–1143 (2009).
33. G. Buzsáki, C. A. Anastassiou, C. Koch, The origin of extracellular fields and currents — EEG, ECoG, LFP and spikes. *Nat. Rev. Neurosci.* **13**, 407–420 (2012).
34. C. Barba, G. Barbati, L. Minotti, D. Hoffmann, P. Kahane, Ictal clinical and scalp-EEG findings differentiating temporal lobe epilepsies from temporal "plus" epilepsies. *Brain* **130**, 1957–1967 (2007).
35. F. Bartolomei, D. Cosandier-Rimele, A. McGonigal, S. Aubert, J. Régis, M. Gavaret, F. Wendling, P. Chauvel, From mesial temporal lobe to temporoperisylvian seizures: A quantified study of temporal lobe seizure networks. *Epilepsia* **51**, 2147–2158 (2010).
36. G. M. Edelman, J. A. Gally, Degeneracy and complexity in biological systems. *Proc. Natl. Acad. Sci. U.S.A.* **98**, 13763–13768 (2001).
37. V. Jirsa, *Structured Flows on Manifolds as Guiding Concepts in Brain Science* (Springer, 2020).
38. A. Li, C. Huynh, Z. Fitzgerald, I. Cajigas, D. Brusko, J. Jagid, A. O. Claudio, A. M. Kanner, J. Hopp, S. Chen, J. Haagensen, E. Johnson, W. Anderson, N. Crone, S. Inati, K. A. Zaghloul, J. Bulacio, J. Gonzalez-Martinez, S. V. Sarma, Neural fragility as an EEG marker of the seizure onset zone. *Nat. Neurosci.* **24**, 1465–1474 (2021).
39. B. Yang, M. Li, W. Tang, W. Liu, S. Zhang, L. Chen, J. Xia, Dynamic network biomarker indicates pulmonary metastasis at the tipping point of hepatocellular carcinoma. *Nat. Commun.* **9**, 678 (2018).
40. J. C. Bulacio, L. Jehi, C. Wong, J. Gonzalez-Martinez, P. Kotagal, D. Nair, I. Najm, W. Bingaman, Long-term seizure outcome after resective surgery in patients evaluated with intracranial electrodes. *Epilepsia* **53**, 1722–1730 (2012).
41. I. Sarikaya, PET studies in epilepsy. *Am. J. Nucl. Med. Mol. Imaging* **5**, 416–430 (2015).
42. K. J. Friston, B. Li, J. Daunizeau, K. E. Stephan, Network discovery with DCM. *Neuroimage* **56**, 1202–1221 (2011).
43. G. K. Cooray, B. Sengupta, P. K. Douglas, K. Friston, Dynamic causal modelling of electrographic seizure activity using Bayesian belief updating. *Neuroimage* **125**, 1142–1154 (2016).
44. M. Papadopoulou, M. Leite, P. van Mierlo, K. Vonck, L. Lemieux, K. Friston, D. Marinazzo, Tracking slow modulations in synaptic gain using dynamic causal modelling: Validation in epilepsy. *Neuroimage* **107**, 117–126 (2015).
45. I. A. Nissen, A. P. Millán, C. J. Stam, E. C. W. van Straaten, L. Douw, P. J. W. Pouwels, S. Idema, J. C. Baayen, D. Velis, P. Van Mieghem, A. Hillebrand, Optimization of epilepsy surgery through virtual resections on individual structural brain networks. *Sci. Rep.* **11**, 19025 (2021).
46. L. G. Kini, J. M. Bernabei, F. Mikhail, P. Hadar, P. Shah, A. N. Khambhati, K. Oechsel, R. Archer, J. Boccanfuso, E. Conrad, R. T. Shinohara, J. M. Stein, S. Das, A. Kheder, T. H. Lucas, K. A. Davis, D. S. Bassett, B. Litt, Virtual resection predicts surgical outcome for drug-resistant epilepsy. *Brain* **142**, 3892–3905 (2019).
47. L. Junges, M. A. Lopes, J. R. Terry, M. Goodfellow, The role that choice of model plays in predictions for epilepsy surgery. *Sci. Rep.* **9**, 7351 (2019).
48. M. O. Baud, J. K. Kleen, E. A. Mirro, J. C. Andrechak, D. King-Stephens, E. F. Chang, V. R. Rao, Multi-day rhythms modulate seizure risk in epilepsy. *Nat. Commun.* **9**, 88 (2018).
49. P. J. Karoly, V. R. Rao, N. M. Gregg, G. A. Worrell, C. Bernard, M. J. Cook, M. O. Baud, Cycles in epilepsy. *Nat. Rev. Neurol.* **17**, 267–284 (2021).
50. M. J. Cook, P. J. Karoly, D. R. Freestone, D. Himes, K. Leyde, S. Berkovic, T. O'Brien, D. B. Grayden, R. Boston, Human focal seizures are characterized by populations of fixed duration and interval. *Epilepsia* **57**, 359–368 (2016).
51. K. Zilles, K. Amunts, Cytoarchitectonic and receptorarchitectonic organization in Broca's region and surrounding cortex. *Curr. Opin. Behav. Sci.* **21**, 93–105 (2018).

52. K. Amunts, C. Lepage, L. Borgeat, H. Mohlberg, T. Dickscheid, M.-E. Rousseau, S. Bludau, P.-L. Bazin, L. B. Lewis, A.-M. Oros-Peusquens, N. J. Shah, T. Lippert, K. Zilles, A. C. Evans, BigBrain: An ultrahigh-resolution 3D human brain model. *Science* **340**, 1472–1475 (2013).
53. B. Ridley, A. Marchi, J. Wirsich, E. Soulier, S. Confort-Gouny, L. Schad, F. Bartolomei, J.-P. Ranjeva, M. Guye, W. Zaaraoui, Brain sodium MRI in human epilepsy: Disturbances of ionic homeostasis reflect the organization of pathological regions. *Neuroimage* **157**, 173–183 (2017).
54. B. Frauscher, N. von Ellenrieder, R. Zelmann, I. Doležalová, L. Minotti, A. Olivier, J. Hall, D. Hoffmann, D. K. Nguyen, P. Kahane, F. Dubeau, J. Gotman, Atlas of the normal intracranial electroencephalogram: Neurophysiological awake activity in different cortical areas. *Brain* **141**, 1130–1144 (2018).
55. W. E. Huifang, T. Paul, V. Jirsa, VEP_workflow_simulatedData (2022); https://zenodo.org/record/5816706#.Y7uvc3ZBy3A.
56. H. E. Wang, M. Woodman, P. Triebkorn, J.-D. Lemaréchal, J. Jha, B. Dollomaja, A. Vattikonda, V. Sip, M. Hashemi, V. Jirsa, Codes: Patient-specific digital neuroscience workflow for epilepsy (2022); https://doi.org/10.5281/zenodo.7154400.
57. J.-D. Tournier, R. Smith, D. Raffelt, R. Tabbara, T. Dhollander, M. Pietsch, D. Christiaens, B. Jeurissen, C.-H. Yeh, A. Connelly, MRtrix3: A fast, flexible and open software framework for medical image processing and visualisation. *Neuroimage* **202**, 116137 (2019).
58. J.-D. Tournier, F. Calamante, A. Connelly, MRtrix: Diffusion tractography in crossing fiber regions. *Int. J. Imaging Syst. Technol.* **22**, 53–66 (2012).
59. J.-D. Tournier, F. Calamante, A. Connelly, Robust determination of the fibre orientation distribution in diffusion MRI: Non-negativity constrained super-resolved spherical deconvolution. *Neuroimage* **35**, 1459–1472 (2007).
60. J.-D. Tournier, F. Calamante, A. Connelly, Improved probabilistic streamlines tractography by 2nd order integration over fibre orientation distributions, in *Proceedings of the International Society for Magnetic Resonance in Medicine*, Stockholm, Sweden, 1 to 7 May 2010, p. 1670.
61. S. M. Villalon, R. Paz, N. Roehri, S. Lagarde, F. Pizzo, B. Colombet, F. Bartolomei, R. Carron, C.-G. Bénar, EpiTools, a software suite for presurgical brain mapping in epilepsy: Intracerebral EEG. *J. Neurosci. Methods* **303**, 7–15 (2018).
62. T. Proix, F. Bartolomei, P. Chauvel, C. Bernard, V. K. Jirsa, Permittivity coupling across brain regions determines seizure recruitment in partial epilepsy. *J. Neurosci.* **34**, 15009–15021 (2014).
63. M. D. Hoffman, A. Gelman, NThe No-U-turn sampler: Adaptively setting path lengths in Hamiltonian Monte Carlo. *J. Mach. Learn. Res.* **15**, 1593–1623 (2014).
64. J. Bancaud, J. Talairach, C. Schaub, G. Szikla, Stereotactic functional exploration of the epilepsies of the supplementary area of the mesial surfaces of the hemispheres. *Electroencephalogr. Clin. Neurophysiol.* **14**, 788 (1962).
65. H. O. Lüders, I. Najm, D. Nair, P. Widdess-Walsh, W. Bingman, The epileptogenic zone: General principles. *Epileptic Disord.* **8**, S1–S9 (2006).
66. M. Betancourt, Calibrating model-based inferences and decisions. arXiv:1803.08393 (2018).
67. S. Lagarde, S. Buzori, A. Trebuchon, R. Carron, D. Scavarda, M. Milh, A. McGonigal, F. Bartolomei, The repertoire of seizure onset patterns in human focal epilepsies: Determinants and prognostic values. *Epilepsia* **60**, 85–95 (2019).

Acknowledgments: We thank C. Filipescu for help with data collection; E. Garnier for data management; D. Scavarda and R. Carron for the surgical management of included patients; and A. Tresbuchon, A. McGonigal, and N. Villeueuve for the clinical management of some included patients. We thank M. Betancourt for consulting on Bayesian analysis and Stan application. **Funding:** V.J., M.G., and F.B. receive research funding from the French National Research Agency (ANR) as part of the second "Investissements d'Avenir" program (ANR-17-RHUS-0004, EPINOV). V.J. and M.G. receive funding from the European Union's Horizon 2020 Framework Programme for Research and Innovation under the specific grant agreement no. 945539 (Human Brain Project SGA3). **Author contributions:** V.J., F.B., and M.G. conceived the study. V.J. and H.E.W. formulated and developed the methodology. H.E.W., V.J., P.T., J.J., J.-D.L., M.W., A.N.V., B.D., M.H., and S.M.V. developed the software. H.E.W. and J.M. performed data analysis. H.E.W. and P.T. created visualizations. H.E.W., P.T., and V.J. wrote the original draft. All authors contributed to manuscript editing. **Competing interests:** V.J., F.B., and M.G. hold a patent "Method of modulating epileptogenicity in a patient's brain (patent no. 11191476)". V.J., F.B., H.E.W., M.W., and M.G. are shareholders of VB-Tech (Virtual Brain Technologies). The other authors declare that they have no competing interests. **Data and materials availability:** All data associated with this study are present in the paper or the Supplementary Materials. Example data that support the findings of this study are available in Zenodo (https://doi.org/10.5281/zenodo.5816706) (*55*). These data include a patient's preprocessed anatomical and high-resolution functional simulation data. The patient raw datasets cannot be made publicly available due to the data protection concerns regarding potentially identifying and sensitive patient information. Interested researchers may access the datasets by contacting the corresponding authors. The VEP pipeline code used in this study is available from Zenodo (https://doi.org/10.5281/zenodo.7154400) (*56*).

Submitted 7 March 2022
Resubmitted 28 August 2022
Accepted 4 January 2023
Published 25 January 2023
10.1126/scitranslmed.abp8982

Science Translational Medicine

Delineating epileptogenic networks using brain imaging data and personalized modeling in drug-resistant epilepsy

Huifang E. Wang, Marmaduke Woodman, Paul Triebkorn, Jean-Didier Lemarechal, Jayant Jha, Borana Dollomaja, Anirudh Nihalani Vattikonda, Viktor Sip, Samuel Medina Villalon, Meysam Hashemi, Maxime Guye, Julia Makhalova, Fabrice Bartolomei, and Viktor Jirsa

Sci. Transl. Med., **15** (680), eabp8982.
DOI: 10.1126/scitranslmed.abp8982